Research article

Qian Ma, Qiao Ru Hong, Xin Xin Gao, Hong Bo Jing, Che Liu, Guo Dong Bai, Qiang Cheng and Tie Jun Cui*

Smart sensing metasurface with self-defined functions in dual polarizations

https://doi.org/10.1515/nanoph-2020-0052
Received January 24, 2020; revised February 27, 2020; accepted March 20, 2020

Abstract: For the intelligence of metamaterials, the sensing mechanism and programmable reaction units are two important components for self-recognition and determination. However, their realization still face great challenges. Here, we propose a smart sensing metasurface to achieve self-defined functions in the framework of digital coding metamaterials. A sensing unit that can simultaneously process the sensing channel and realize phase-programmable capability is designed by integrating radio frequency (RF) power detector and PIN diodes. Four sensing units distributed on the metasurface aperture can detect the microwave incidences in the *x*- and *y*-polarizations, while the other elements can modulate the reflected phase patterns under the control of a field programmable gate array (FPGA). To validate the performance, three schemes containing six coding patterns are presented and simulated, after which two of them are measured, showing good agreements with designs. We envision that this work may motivate studies on smart metamaterials with high-level recognition and manipulation.

Keywords: programmable metasurface; sensing metasurface; dual-polarization; smart metasurface.

1 Introduction

Metamaterials are artificial structures of periodic or non-periodic arrays with subwavelength unit cells, which can be engineered to obtain compelling electromagnetic (EM) properties [1–3] by means of effective permittivity and permeability that do not exist in nature, such as negative permittivity, negative permeability and negative index of refraction. The metamaterials based on effective medium theory have attracted a great surge of interest due to their powerful abilities in manipulating the EM waves. Based on the concept, numerous novel applications have been proposed, including perfect imaging [4], super lens [5] and invisibility cloaking [6]. To explore the connection between physical fields and information science, the concepts of digital-coding metasurfaces and programmable metasurfaces have been proposed [7], opening up a new perspective for digital representation [8, 9] and informational operations [10–12] on the physical world with metamaterials. By digitizing the specifically physical parameters, the digital elements of "0" and "1" can represent the phase difference [13], amplitude [14, 15] and polarization [16] of the EM waves, thus enabling the direct modulations of EM waves and digital information by applying the field-programmable gate array (FPGA) [7]. Due to the superior performance and concise architecture, the digital-coding metasurfaces have realized various applications on space-time modulations [17, 18], communication [19, 20] and imaging [21, 22].

As a higher-level stage, the intelligence of metamaterials is imminently demanded for more customized and special functionalities. One pivotal step is sensing and collecting the data from the environment, which leads to the diverse sensing mechanisms of metamaterials, such as resonance spectrum [23–31], polarizations [31] and mechanicalness [32]. However, these sensing works only aim at converting the object into a measurable indicator, thus they rely on the measuring instruments and lack a direct signal feedback for metasurface reactions. More importantly, these metasurfaces are unable to actively manipulate the EM fields. To combine the advantages of programmable metasurfaces and sensing capabilities, a smart metasurface architecture integrated with sensors and feedback channel has been presented [33], realizing the self-adaptive controls of EM waves without using

***Corresponding author: Tie Jun Cui,** State Key Laboratory of Millimeter Wave, Southeast University, Nanjing 210096, China, e-mail: tjcui@seu.edu.cn
Qian Ma, Qiao Ru Hong, Xin Xin Gao, Hong Bo Jing, Che Liu, Guo Dong Bai and Qiang Cheng: State Key Laboratory of Millimeter Wave, Southeast University, Nanjing 210096, China.
https://orcid.org/0000-0002-4662-8667 (Q. Ma)

Published online April 22, 2020

human instructions. Furthermore, by integrating light-collectors, the digital coding metasurface was successfully equipped with visible-light detectors to manipulate the microwave [34]. A similar mechanism was also realized by using the shape memory material [35, 36], combining thermal and microwave responses.

However, these kinds of metasurfaces were designed to sense and manipulate different objects (e.g. spatial motions and scattering fields [33]), or different bands, or different fields (e.g. microwave versus visible light [34] or thermal fields [35]), which limit the further intelligence because of the missing information on the tailoring target. In many realistic situations, the metasurface should sense and react on the same object, such as the microwave scattering fields, thereby suggesting more meaning and application potentials for smart metamaterials. Considering this point, we propose in the current work a metasurface to simultaneously achieve the sensing and manipulation on the microwave scattering fields. By designing a special unit structure and integrating detecting circuits, the programmable metasurface is able to sense and modulate the 1-bit phases in the dual polarizations. Numerical simulations and experimental measurements show good consistency, validating the proposed smart sensing metasurface.

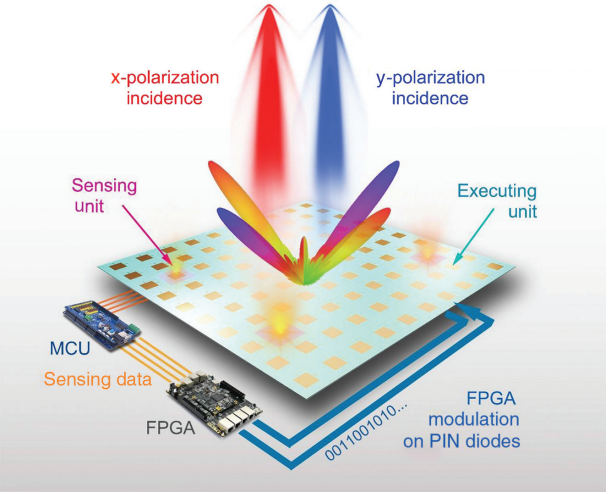

Figure 1: The schematic of the presented smart sensing metasurface.
The sensing unit distributed on the metasurface can detect the incident waves in the *x*- and *y*-polarizations and send the sesing data to the FPGA for self-defined functions in the two polarizations.

2 Results and discussion

We propose a smart sensing metasurface, which evolved from the phase-programmable metasurface, with self-recognitions and manipulations on the reflecting phase patterns on dual polarizations. Figure 1 provides a schematic of the presented metasurface, which is composed of the sensing units (S-units) and executing units (E-units). Under the incidences of different polarizations, the sensing units are able to recognize the incident power levels and transmit the data to the microcontroller unit (MCU) for digitizing. After collecting the data, the FPGA is able to determine the coding patterns independently on the specific polarization and drive the executing units to realize the desired scattering fields. By integrating the PIN diodes on two orthogonal directions, both the S-units and E-units can modulate the phase responses independently, which guarantee the excellent capabilitis to control the scattering fields. According to the power levels from the sensing data, the metasurface can generate various scattering fields based on the pre-designed algorithm [33]. Consequently, the functionalities can be arbitrarily grouped and become reprogrammable depending on the specific design.

To achieve the dual-polarization phase modulations, a patch structure embedded with PIN diodes (MACOM 14020) is applied in the element design, as shown in Figure 2A. Two PIN diodes are connected to the central patch through two metal bars along the *x*- and *y*-axes to tailor the phases in the respective orthogonal linear polarizations. The sandwich-like element structure is piled up with two substrate layers (FR4, the dielectric constant is 4.4) with the same thickness (1.5 mm). The dimension parameters in Figure 2 are given a follows: a = 30 mm, b = 13.6 mm, c = 3.1 mm and h = 3.1 mm. Each PIN diode is equivalent to a series RLC model: R = 2.2 Ω, L = 0.4 nH and C = 0 fF when the diode is switched on; and R = 0 Ω, L = 0.4 nH and C = 40 fF when the diode is switched off. The top and bottom views of the sensing unit and executing unit are exhibited in Figure 2B. Meanwhile, the positive side of the PIN diode is conducted with the back-side sector structure for the radio-frequency (RF) signal isolation and DC voltage bias. For the S-unit, a via-hole penetrates from the top metal patch to the bottom side to induce the RF energy into the detecting circuit. The position of the via-hole determines the sensing polarization of the incidence. We remark that two kinds of S-units are designed for recognizing two polarizations, respectively. In the example shown in Figure 2B, we show an S-unit for the *x*-polarization detection, in which the via-hole is along the *x*-axis.

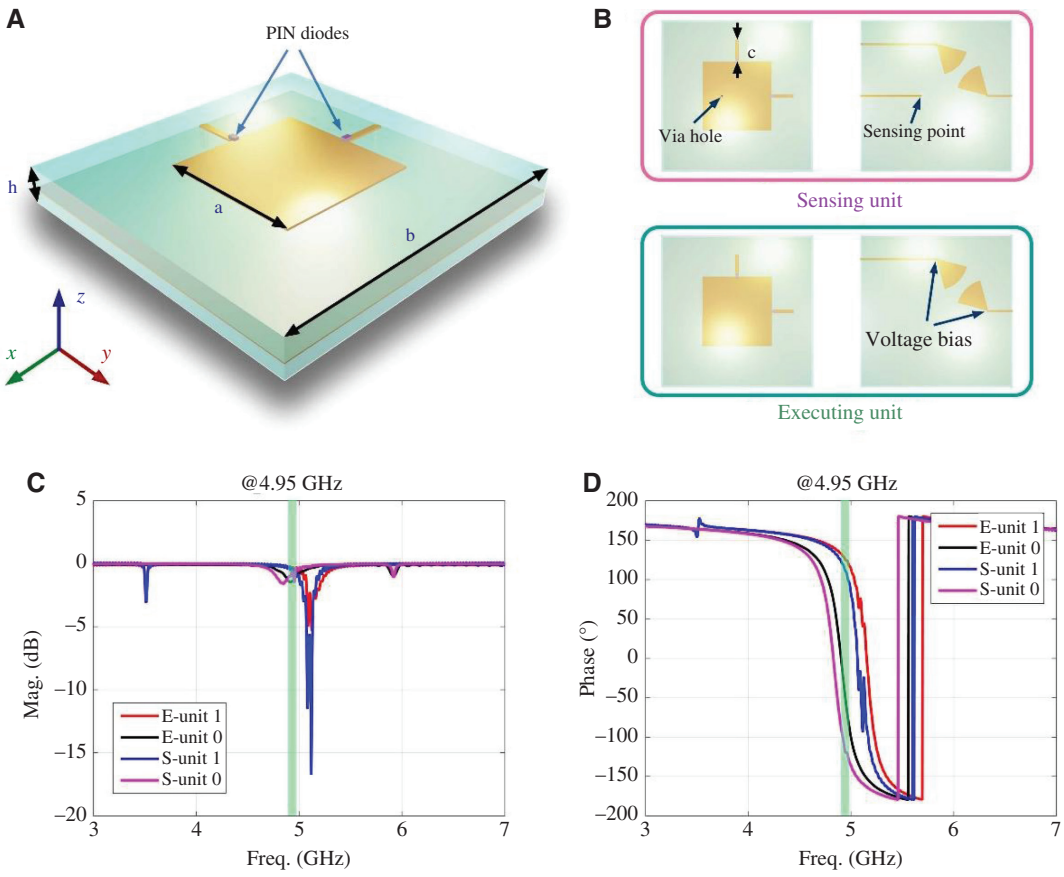

Figure 2: The designed digital coding elements for sensing and executing targets.
(A) The detailed structure of the coding element. (B) The top and bottom views of the sensing and executing units. (C, D) The reflected magnitude and phase responses of the executing and sensing units when the PIN diode is switched on and off.

The element simulations are performed using commercial software, CST Microwave Studio. We list the simulated magnitude and phase responses of the reflected wave in Figure 2C and D, respectively. Given that the structure of the presented element is symmetrical along the *x*- and *y*-axes, for the *x*- and *y*-polarized diode modulations, the phase modulations for the *x*- and *y*-polarized incidences are the same. Consequently, we only give the results with the on-off situations of the PIN diode along the *x*-axis. From Figure 2C, we observe that the reflected magnitude is almost around 0 dB at the central frequency 4.95 GHz, marked in green color. Figure 2D illustrates the phase responses of the S-unit and E-unit when the diode is on or off, where we can observe a slight deviation of the two kinds of units. At 4.95 GHz, the phase responses of the E-unit are 124° and –56°, while the results of the S-unit are 109° and –120°. The operating bandwidth is about 40 MHz when the phase difference between the 0 and 1 states ranges from 160° to 200°. As the incident angle increases from 0° to 30°, the phase difference at the same frequency decreases from 180° to 160°. In the whole metasurface configuration, we only arrange four S-units among 100 elements. Considering the incidence from a long distance, the sensing unit on any position of a limited-dimension metasurface receives almost the same power level. Hence, we arrange four S-units in the whole metasurface, thereby greatly reducing the cost of components and fabrication difficulty while also promising the same sensing performance.

To clearly present the sensing mechanism of the S-unit, we provide the detailed circuit design for the sensing module, which is mainly composed of an RF power detector, LTC5530 and several peripheral components. The detailed values of these components are listed as follows: R2 = 22k Ω, R3 = 10k Ω, R4 = 10k Ω, C1 = 0.1 uF, C2 = 100 pF and C4 = 39 pF. Here, R3 and R4 are used to control the internal amplifier gain, R2 is a pull-up resistor for enabling the port control, C1 and C2 are the capacitors for power inpuit filtering and C1 is used for matching the input impedence and isolating the DC signal. Each S-unit is equipped with a sensing module to feed back the sensing voltage to FPGA. Figure 3B and C show the

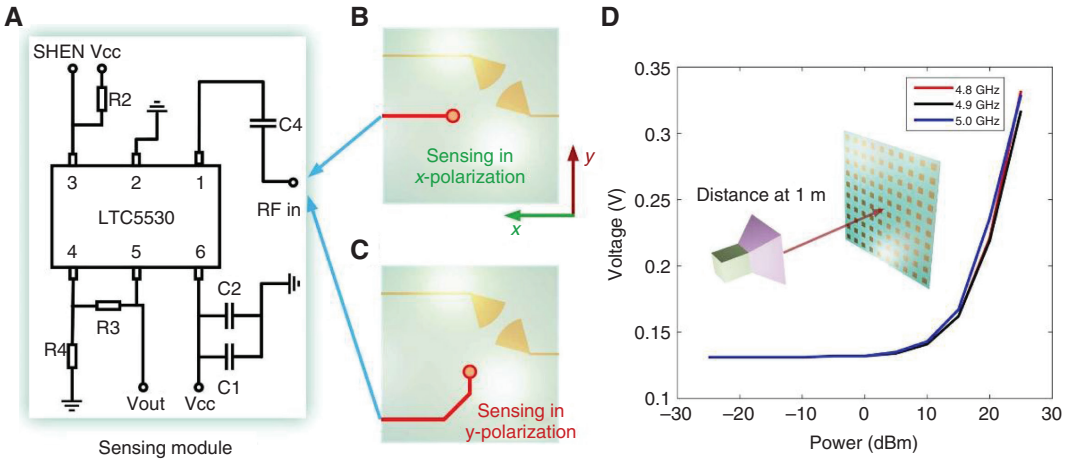

Figure 3: The sensing mechanism of the sensing unit for the *x*- and *y*-polarizations.
(A) The circuit of the sensing module integrated on the sensing unit. (B, C) The bottom views of the sensing units for the *x*- and *y*-polarizations. (D) The measured sensing voltage versus different power levels of the incident wave when the source is placed at 1 m from the metasurface.

bottom views of the S-unit for the *x*- and *y*-polarization sensing, respectively, whose corresponding via-holes are placed along the *x*- and *y*-axes. These via-holes are connected to the related RF input of the sensing module. To obviously show the detecting performance, the measured voltage (from Vout of the sensing module) versus the incident power (when the horn antenna is placed at 1 m away from the metasurface) is presented in Figure 3D. In this measurement, the horn antenna is linked directly to a signal generator, while the sensing module is connected to a voltmeter. When the power level of the signal generator exceeds 10 dBm, the output voltage increases apparently from 0.15 V to 0.3 V, which can be perceived by MCU. According to the feedback voltages, various functionalities are available for designing.

In Figure 4, we present three group schemes, as shown in Figure 4A, D and G, respectively, to illustrate the diverse functions achieved by the smart sensing metasurface when illuminated by distinct polarizations. With independent controls on each unit in two polarizations, we can design distinct 1-bit digital coding patterns for the *x*- and *y*-polarizations simultaneously. Thus, two patterns (Patterns A and B) can be arranged synchronously on the metasurface, reflecting different scattering fields under different polarization incidences. To clearly distinguish the phase codes in two polarizations, we indicate the pattern with four different colors, corresponding to the two phase responses in the two polarizations. In the first scheme, we demonstrate the dual-beam scattering fields with orthogonally propagating directions (along the *x*- and *y*-axes) in two polarizations. Figure 4B and C present the simulated far-field results in the *x*- and *y*-polarizations, in which two obvious scattering beams respectively direct to the *x*- and *y*-axes. Figure 4D exhibits two quad-beam patterns with different deflection angles, produced by chessboard patterns C and D, in which the pattern period length is different, resulting in distinct beam-deflection angles. In Figure 4E and F, the related far-field data are listed, and the quad-beam fields along the *x*- and *y*-axes are clearly observed, respectively. In the third scheme (Figure 4G), the radar-cross-section (RCS) reduction pattern (E) and beam-deflection pattern (F) are grouped. In Figure 4H, an apparent reduction of the reflected energy can be observed. Figure 4I presents dual-beam scattering fields with smaller deflection angles, since the coding sequence has a larger period.

A fabricated metasurface is shown in Figure 5A and B, referring to the top and bottom views. Four S-units with gold-plated technics are clearly observed, in which two of them are used to monitor the *x*-polarization and the others are used to monitor the *y*-polarization. The related detecting circuit is embedded on the bottom side of the metasurface. All bias lines for the elements are placed on the bottom layer and are connected to the FPGA control interface with cable lines. We remark that the processing time from the detection to arranging the phase pattern is about 15.2 us, which can be further reduced by applying the higher-speed ADC and FPGA. Considering that the whole metasurface is mainly composed of E-units, these E-units will almost determine the final far-field patterns. The measuring frequency should be consistent with the frequency point of 180° phase difference of E-unit (4.95GHz in simulation).

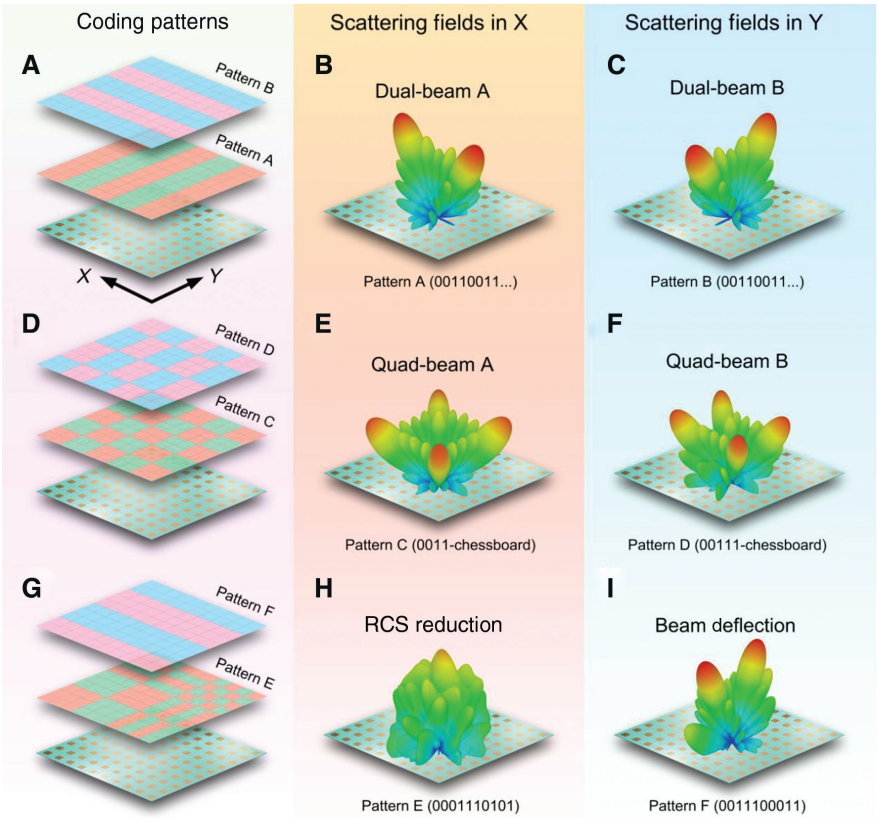

Figure 4: The designed schemes and coding patterns for the *x*- and *y*-polarizations.
(A, D, G) The three schemes for different-polarization incidences, where the patterns for the *x*-polarization is marked in orange and green, and the patterns for the *y*-polarization are marked in blue and pink, for the "0" and "1" states, respectively. (B, E, H) The simulated scattering fields in the *x*-polarization under the corresponding patterns. (C, F, I) The simulated scattering fields in the *y*-polarization under the corresponding patterns.

The metasurface is measured in a standard chamber room, as shown in Figure 5C and D. The metasurface, feeding source and FPGA are fixed on a rotatable table to measure the far-field data on a plane. The feeding horn antenna is set at 1 m away from the metasurface, while the receiving horn is placed at about 10 m from the rotatable table.

To experimentally demonstrate the manipulation performance of the metasurface on the EM fields, we provide the measured far-field results of the coding patterns A, B, E and F in Figure 6, as well as the corresponding simulation results for comparison. To clearly measure the far-field data, the FPGA is set as executing the specific pattern when the sensing units detect a high power level in the *x*- or *y*-polarization. In Figure 6A and B, we show the dual-beam scattering fields in the *x*- and *y*-polarizations, whose coding patterns vary respectively along the *x*- and *y*-axes. The best measured results are collected at 5.2 GHz. The frequency deviation between simulation and measurement mainly results from the finite metasurface dimension as well as the model error of the diode between simulations and reality. The scattering beams at the angles ±30° are clearly observed, thus implying good agreements between simulations and measurements. Another two representative cases (patterns E and F) are listed in Figure 6C and D, which respectively achieve the features of RCS reduction and beam deflection. To clearly illustrate the performance of pattern E, we also provide a simulated field reflected by a perfect electric conductor (PEC). Compared to the PEC plate with the same dimension, the RCS reduction realized by the coding pattern E is about 8.5 dB. Finally, Figure 6D exhibits the beam-deflection case in which the two symmetrical beams at ±21° are obviously detected. The slight deviation to the simulated results is mainly caused by the following reasons: (1) the fabrication error in PCB processing and soldering, (2) the manual operations in the experiments and (3) the imperfect plane wave from the horn antenna. Furthermore, the fluctuating curve of the measured data mainly results from the low magnitude received by the horn antenna because of the finite dimension of the metasurface (about 5 wavelengths) and low-gain horn antenna.

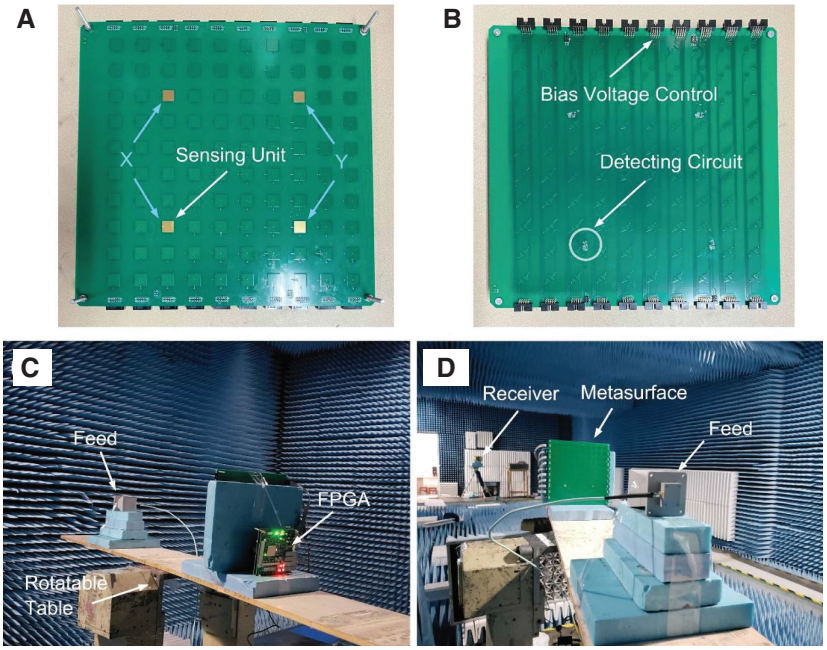

Figure 5: The photographs of the metasurface sample and experiments.
(A, B) The top and bottom views of the fabricated metasurface sample. (C, D) The experiment configuration of the far-field measurements.

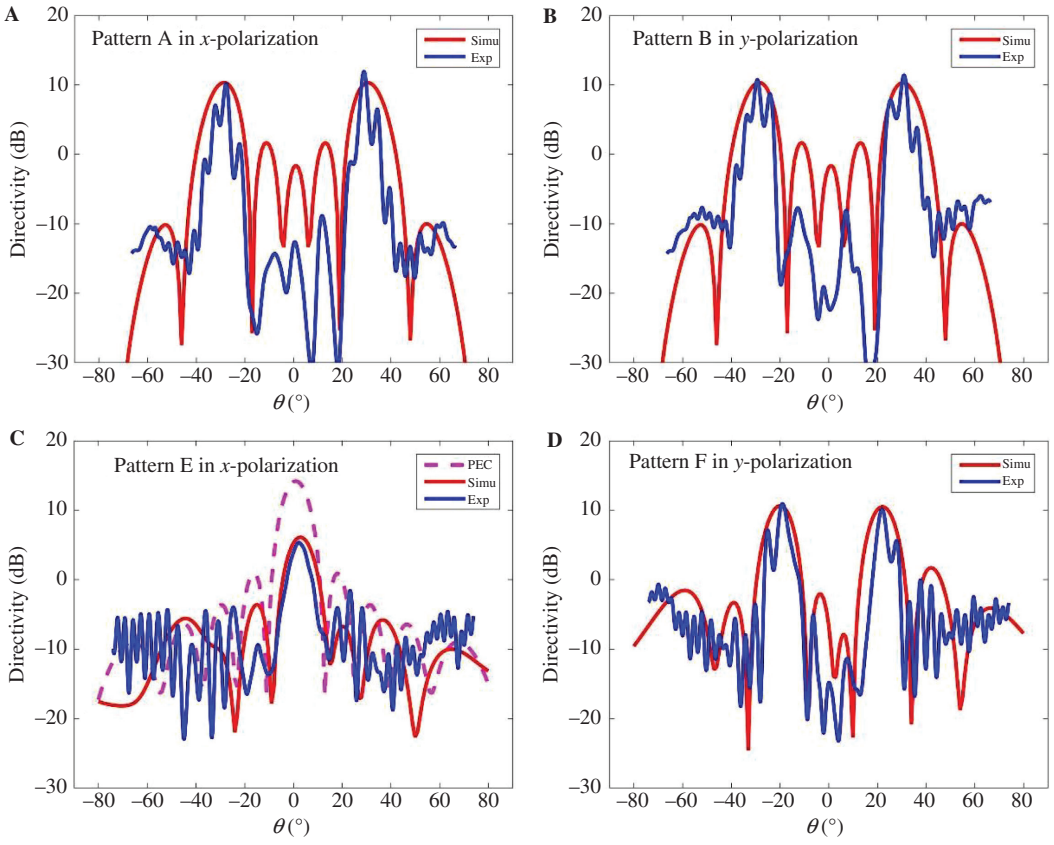

Figure 6: The measured results for coding patterns A, B, E and F, compared to the simulated results.
(A) The simulated and measured data of coding pattern A in the *x*-polarization. (B) The simulated and measured data of coding pattern B in the *y*-polarization. (C) The simulated and measured data of coding pattern E in the *x*-polarization. (D) The simulated and measured data of the coding pattern F in the *y*-polarization.

3 Conclusion

We presented a smart sensing metasurface equipped with the incidence detection and 1-bit digital phase modulation in dual-polarization modes. Two kinds of programmable units, the sensing unit and executing unit, were designed for incident-wave sensing and reflected-field manipulations. Six distinct digital coding patterns for the *x*- and *y*-polarizations were proposed and simulated, where four representative patterns were measured. The experimental results had good agreement with the numerical simulations, further verifying the smart sensing metasurface and the design method. Compared to the previous sensing metasurface and smart metasurface architecture we proposed before, the new smart sensing metasurface is the first to combine the sensing and reaction capabilities for the microwave incidence. By circularly reflecting specific patterns and sensing the EM amplitude distributions, the presented metasurface is able to learn more intelligent imaging and communication applications. We believe that this work will further promote the development of intelligent and cognitive metamaterials according to our conceptions of the next-generation metamaterials [37, 38].

4 Methods

In numerical simulations, we employ the commercial software, CST Microwave Studio. The periodic boundary is applied in the element structure simulations. For the whole metasurface simulations, the open boundary and ideal plane-wave excitation have been applied. For the RCS reduction pattern (Pattern E) design, an optimization algorithm (particle swarm optimization) is applied for optimizing the coding sequence, so as to reduce the maximum scattering power in one dimension. Then the obtained coding sequence is extended to a 2D coding pattern for far-field simulations to test its performance. This whole process may be iteratively excuated to select the best result. In the sensing voltage measurement, an analog signal generator (Agilent E8257D) is applied to emit different power levels. Then, the metasurface sample is fabricated using the printed circuit board (PCB) technology and soldered by the surface mounted technology (SMT). The far-field measurement is performed in a standard microwave chamber room in the C band. A broadband horn antenna is applied as the feeding source. It is worth mentioning that the presented mechanism can be further applied to the transmissive metasurface by designing appropriate structure to integrate a coupling module. The direct connection [15] and coupling sensing [39] are two possible ways to collect the transmitted energy.

Acknowledgments: This work was supported in part by the National Key Research and Development Program of China (2017YFA0700201, 2017YFA0700202 and 2017YFA0700201), in part by the National Natural Science Foundation of China (61631007, 61571117, 61501112, 61501117, 61522106, Funder Id: http://dx.doi.org/10.13039/501100001809, 61731010, 61735010, 61722106, 61701107 and 61701108), in part by the 111 Project (111-2-05) and in part by the Fund for International Cooperation and Exchange of the National Natural Science Foundation of China (61761136007).

Conflicts of interest: There are no conflicts to declare.

References

[1] Veselago VG. The electrodynamics of substances with simultaneously negative values of ε and μ. Soviet Phys Uspekhi 1968;10:509–14.
[2] Pendry JB, Schurig D, Smith DR. Controlling electromagnetic fields. Science 2006;312:1780–2.
[3] Smith DR, Padilla WJ, Vier DC, Nemat-Nasser SC, Schultz S. Composite medium with simultaneously negative permeability and permittivity. Phys Rev Lett 2000;84:4184–7.
[4] Leonhardt U. Perfect imaging without negative refraction. New J Phys 2009;11:093040-1–2.
[5] Pendry JB. Negative refraction makes a perfect lens. Phys Rev Lett 2000;85:3966–9.
[6] Ma Q, Mei ZL, Zhu SK, Jin TY, Cui TJ. Experiments on active cloaking and illusion for laplace equation. Phys Rev Lett 2013;111:173901-1–5.
[7] Cui TJ, Qi MQ, Wan X, Zhao J, Cheng Q. Coding metamaterials, digital metamaterials and programmable metamaterials. Light-Sci Appl 2014;3:e218.
[8] Ma Q, Shi CB, Bai GD, Chen TY, Noor A, Cui TJ. Beam-editing coding metasurfaces based on polarization bit and orbital-angular-momentum-Mode Bit. Adv Opt Mater 2017;5:1700548.
[9] Cui TJ, Liu S, Zhang L. Information metamaterials and metasurfaces. J Mater Chem C 2017;5:3644–68.
[10] Cui TJ, Liu S, Liu L-L. Information entropy of coding metasurface. Light-Sci Appl 2016;5:e16172.
[11] Liu S, Cui TJ, Zhang L, et al. Convolution operations on coding metasurface to reach flexible and continuous controls of Terahertz. Adv Sci 2016;3:1600156.
[12] Wu RY, Shi CB, Liu S, Wu W, Cui TJ. Addition theorem for digital coding metamaterials. Adv Opt Mater 2018;6:1701236.
[13] Wan X, Zhang Q, Chen TY, et al. Multichannel direct transmissions of near-field information. Light-Sci Appl 2019;8:60.
[14] Chen L, Ma Q, Jing HB, et al. Space-energy digital-coding metasurface based on an active amplifier. Phys Rev Appl 2019;11:054051-1–6.

[15] Ma Q, Chen L, Jing HB, et al. Controllable and programmable nonreciprocity based on detachable digital coding metasurface. Adv Opt Mater 2019;7:1901285.
[16] Tao Z, Wan X, Pan BC, et al. Reconfigurable conversions of reflection, transmission, and polarization states using active metasurface. Appl Phys Lett 2017;110:121901-1–5.
[17] Zhang L, Chen XQ, Liu S, et al. Space-time-coding digital metasurfaces. Nat Commun 2018;9:4334.
[18] Dai JY, Zhao J, Chen Q, Cui TJ. Independent control of harmonic amplitudes and phases via a time-domain digital coding metasurface. Light-Sci Appl 2018;7:90.
[19] Cui TJ, Liu S, Bai GD, Ma Q. Direct transmission of digital message via programmable coding metasurface. Research 2019;2019:2584509.
[20] Zhao J, Yang X, Dai JY, et al. Programmable time-domain digital-coding metasurface for non-linear harmonic manipulation and new wireless communication systems. Nat Scie Rev 2019;6:231–8.
[21] Li L, Cui TJ, Ji W, et al. Electromagnetic reprogrammable coding-metasurface holograms. Nat Commun 2017;8:197.
[22] Li L, Ruan H, Liu C, et al. Machine-learning reprogrammable metasurface imager. Nat Commun 2019;10:1082.
[23] Gupta M, Srivastava YK, Manjappa M, et al. Sensing with toroidal metamaterial. Appl Phys Lett 2017;110:121108-1–5.
[24] Chen J, Nie H, Tang C, et al. Highly sensitive refractive-index sensor based on strong magnetic resonance in metamaterials. Appl Phys Express 2019;12:052015.
[25] Tan S, Yan F, Wang W, et al. Ultrasensitive sensing with three-dimensional terahertz metamaterial absorber. J Optics 2018;20:055101.
[26] Abdolrazzaghi M, Daneshmand M, Iyer AK. Strongly enhanced sensitivity in planar microwave sensors based on metamaterial coupling. IEEE Trans Microw Theory Techn 2018;66:1843–55.
[27] Wu Z, Chen X, Wang M, et al. High-performance ultrathin active chiral metamaterials. ACS Nano 2018;12:5030–41.
[28] Rahman MN, Islam MT, Samsuzzaman M. Design and analysis of a resonator based metamaterial for sensor applications. Microw Opt Techn Lett 2018;60:694–8.
[29] Garoli D, Calandrini E, Giovannini G, et al. Nanoporous gold metamaterials for high sensitivity plasmonic sensing. Nanoscale Horiz 2019;4:1153–7.
[30] Xu W, Xie L, Ying Y. Mechanisms and applications of terahertz metamaterial sensing: a review. Nanoscale 2017;9:13864–78.
[31] Pelzman C, Cho SY. Plasmonic metasurface for simultaneous detection of polarization and spectrum. Opt lett 2016;41:1213–6.
[32] Jiang Y, Liu Z, Matsuhisa N, et al. Auxetic mechanical metamaterials to enhance sensitivity of stretchable strain sensors. Adv Mater 2018;30:1706589.
[33] Ma Q, Bai GD, Jing HB, Yang C, Li L, Cui TJ. Smart metasurface with self-adaptively reprogrammable functions. Light-Sci Appl 2019;8:98.
[34] Zhang XG, Tang WX, Jiang WX, et al. Light-controllable digital coding metasurfaces. Adv Sci 2018;5:1801028.
[35] Li J, Bai LY. DNA Nanotechnology:A metamaterial with memory. Nat Nano. 2012;7:773–4.
[36] Nicolaou ZG, Motter AE. Mechanical metamaterials with negative compressibility transitions. Nat Mater. 2012;11:608–13.
[37] Cui TJ, Liu S, Zhang L. Information metamaterials and metasurfaces. J Mater Chem C 2017;5:3644–68.
[38] Liu S, Cui TJ. Concepts, working principles, and applications of coding and programmable metamaterials. Adv Opt Mater 2017;5:22.
[39] Li Y, Lin J, Guo H, Sun W, Xiao S, Zhou L. A tunable metasurface with switchable functionalities:From perfect transparency to perfect absorption. Adv Opt Mater 2020;2019:1901548.